Impacts of Polarimetric Radar Data Assimilation on Typhoon Rainfall Nowcasting

Chih-Chien Tsai
National Science and Technology Center for Disaster Reduction

Abstract

For a goal to enhance the accuracy of rainfall nowcasts for the case of super Typhoon Soudelor (2015), this study employs a Weather Research and Forecasting (WRF) local ensemble transform Kalman filter (LETKF) radar assimilation system to assess possible benefits from assimilating polarimetric radar observations. A series of radar data assimilation experiments with various combinations of assimilated radar variables and a control experiment without radar data assimilation are carried out for the most intense period near landfall and verified against radar and rain gauge observations. The results show that almost all radar data assimilation experiments have more accurate rainfall nowcasts than the control experiment, especially during the initial 3 hours, but cannot alter the evolution trend governed by the synoptic-scale forcing. Assimilating specific differential phase results in more accurate lower-troposphere analyses and rainfall nowcasts in convective rainfall areas than assimilating reflectivity. Assimilating solely differential reflectivity on top of radial velocity leads to the degradation of rainfall nowcasts, attributable to unreliable background error correlations between differential reflectivity and updated variables especially in the upper troposphere. On top of assimilating both radial velocity and reflectivity, the additional assimilation of specific differential phase still brings significant improvement and the negative impact of differential reflectivity is less influential.

Keywords: rainfall nowcast, polarimetric radar, data assimilation, observation operator, differential reflectivity, specific differential phase

1. Introduction

For radar data assimilation, the accuracy of analyses and consequent rainfall nowcasts largely depends on three key factors: the cloud microphysical parameterization scheme of the model, the assimilation scheme, and the radar observations. Further rainfall nowcast improvement ought to be achievable if the microphysical scheme, assimilation scheme, or radar observations are more advanced. In contrast to single-moment bulk microphysical schemes, numerous studies demonstrated that double-moment bulk, triple-moment bulk, and spectral bin microphysical schemes, which give higher degrees of freedom to hydrometeor size distributions, can simulate more realistic polarimetric radar signatures for the cases of supercells (Putnam et al. 2017a), mesoscale convective systems (Putnam et al. 2017a, b), and hurricanes (Brown et al. 2016). As for the assimilation scheme, it has been generally accepted that the schemes considering flow-dependent background error covariances, such as the four-dimensional variational scheme, ensemble Kalman filter, hybrid scheme, and particle filter, give higher accuracy because they better describe the errors of the day with higher computational costs. Recently, Putnam et al. (2019) demonstrated that the assimilation of polarimetric radar observations in addition to radial velocity and reflectivity improves the cloud microphysical state estimation and mid-level mesocyclone.

Among polarimetric radar variables, differential reflectivity and specific differential phase are the ones suitable for data assimilation owing to their dependence on certain quantitative properties of hydrometeors. Differential reflectivity mainly depends on the shape and size of hydrometeors; specific differential phase additionally depends on the number concentration and is more linearly proportional to the rain rate. Motivated by the case of Typhoon Soudelor (2015) which damaged an S-band polarimetric radar in Taiwan, this study incorporates a polarimetric radar observation operator into the Weather Research and Forecasting (WRF) local ensemble transform Kalman filter (LETKF; Hunt et al. 2007) radar assimilation system developed in Tsai et al. 2014 and assesses how polarimetric radar data assimilation affects rainfall nowcasts for a real super typhoon case.

2. Methodology

Tsai et al. 2014 demonstrated the capability of the WRF-LETKF radar assimilation system to improve rainfall nowcasts by assimilating radial velocity and reflectivity. In this study, this system is employed again, but coupled with a later version V4.0 of the Advanced Research WRF model and a refined observation operator based on Jung et al. (2008a) to address the challenge of real-case polarimetric radar data assimilation. Figure 1 shows the simulation domains of two grids with two-way interaction. There are 45 vertical eta levels with a top of 30 hPa. The physics schemes in use include the WDM6 microphysical scheme, RRTM longwave radiation scheme, Goddard shortwave radiation scheme, MM5 surface layer scheme, Noah land surface model, YSU planetary boundary layer scheme, and Kain-Fritsch cumulus parameterization scheme.

The configuration of LETKF in this study is largely inherited from Tsai et al. 2014, which is optimized for the typhoon scenario. Applying the mixed localization method, which was first proposed in Tsai et al. 2014, the horizontal covariance localization radii are 36 km for u and v and 12 km for the other updated variables. The vertical covariance localization radius is uniformly 4 km. An ensemble size of 40 is used, and a fixed multiplicative covariance inflation factor of 1.08 is used.

The polarimetric radar data used in this study come from the RCWF S-band polarimetric radar of the Central Weather Bureau (Fig. 1). RCWF observations are thinned and interpolated to 19 constant altitude plan position indicator altitudes ranging from 1 to 10 km at a 3-km horizontal resolution and 0.5-km vertical resolution prior to data assimilation. Observation errors are given as 1 m s^{-1} for radial velocity, 2 dBZ for reflectivity, 0.2 dB for differential reflectivity, and 0.5° km^{-1} for specific differential phase referring to Jung et al. (2008b).

3. Typhoon Soudelor (2015)

Soudelor was the most devastating tropical cyclone in the Northwest Pacific region in 2015. Its westbound best track analyzed by the Central Weather Bureau is shown in Fig. 1. At 2000 UTC 7 August, the eye of Soudelor is located 110 km south of RCWF (Fig. 2a). The northern semicircle of Soudelor, the so-called dangerous semicircle, consists of several huge rainbands with reflectivity reaching 50 dBZ. In contrast, fewer rainbands only close to the eye are evident in the southern semicircle, and the most inner one features a significant amount of large raindrops distinguished by high differential reflectivity and specific differential phase values reaching 2.7 dB and 1.8° km^{-1}, respectively (Figs. 2b, c). The values inside the northern huge rainbands are lower over the ocean but increased over the land of Taiwan, especially specific differential phase. This suggests that orographic lifting affects rainbands moving toward terrain and results in stronger convection and rainfall. Co-polar correlation coefficient values are mostly higher than 0.98 within a range of 170 km but decrease beyond (Fig. 2d). This indicates the melting layer above 4-km altitude and the necessity of handling mixed-phase hydrometeors in the observation operator. Heavy rainfall areas labeled A–C that occur on windward slopes in northern Taiwan are visible with 3-h accumulations exceeding 150 mm during 2000–2300 UTC 7 August (Fig. 3a). Their locations correspond well to each rainband. In the next 3 hours, the rainfall decreases in northern Taiwan but increases in central Taiwan (area D in Fig. 3b) as the center of Soudelor gradually moves through central Taiwan. Area A receives a 6-h maximum accumulation of 393 mm (Fig. 3c).

4. Data assimilation experiments

A series of data assimilation experiments are carried out to investigate the sensitivities of rainfall nowcast performance to polarimetric radar data. Figure 4 shows the schematic design of these experiments, aiming at improving the 6-h deterministic rainfall nowcast for the most intense period during 2000 UTC 7 August – 0200 UTC 8 August. NoDA is a deterministic control experiment initialized with a Global Forecast System 0.25-deg forecast at 1200 UTC 7 August. DA represents all experiments that assimilate RCWF observations. The initial 40-member ensemble is perturbed around the NoDA initial condition for LETKF assimilation cycles. After a 6-h ensemble spin-up, nine assimilation cycles at a 15-min interval are performed, and then the analysis ensemble mean is used to generate the deterministic nowcast.

This study focuses on the sensitivities of rainfall nowcasts to individual radar variables, and therefore various combinations of radar variables are constructed for the data assimilation experiments as listed in Table 1. Uppercase V, Z, D, and K in the experiment name stand for assimilating radial velocity, reflectivity, differential reflectivity, and specific differential phase, respectively.

5. Discussions

As a benchmark without radar data assimilation, NoDA is initialized at 1200 UTC 7 August which is 8 hours earlier than the start time (T0, 2000 UTC) of the targeted deterministic nowcast. This is operationally realistic because the next Global Forecast System forecast at 1800 UTC is not available yet at T0 for data latency. The performance in NoDA at T0 is examined by comparing reflectivity, differential reflectivity, and specific differential phase fields (Figs. 5d–f) with RCWF observations (Figs. 5a–c). NoDA predicts the typhoon center and rainband structure reasonably well. While simulated reflectivity, differential reflectivity, and specific differential phase fields exhibit discrete multiple rainbands, the spatial coverage of weak rainfall is underestimated compared to the observations where the gaps between typhoon rainbands are filled with low values. All three fields in NoDA reveal underestimation north of the eye but overestimation west and south of the eye. This inconsistent pattern leads to incorrect rainfall evolution during the deterministic nowcast. The initial 3-h accumulation reveals underestimation in heavy rainfall

area A but overestimation in area C (Fig. 3d). The final 3-h accumulation reveals underestimation throughout areas A–C (as the underestimated rainbands north of the eye move over land) but overestimation in area D. For quantitative verification, the root-mean-square errors and spatial correlation coefficients of hourly rainfall accumulations against observed rainfall within the radar coverage are shown in Fig. 6. NoDA has a minimum root-mean-square error of 11.6 mm and maximum spatial correlation coefficient of 0.80 in the first hour, and then the coefficient has a decreasing trend that indicates the gradual loss of rainfall pattern predictability with forecast time.

Besides examining horizontal distributions, the overall vertical distribution of radar variables at T0 is also examined using contoured frequency by altitude diagrams within the radar coverage, which are separated into convective rainfall areas defined by reflectivity > 40 dB*Z* at 3-km altitude (Fig. 7) and stratiform rainfall areas defined by 10 dB*Z* < reflectivity < 30 dB*Z* at 3-km altitude (Fig. 8). For the observations, reflectivity in convective rainfall areas has a narrow distribution with the median value around 40–44 dB*Z* in the lower troposphere (below 5-km altitude) and wider distribution with the median decreasing more rapidly with height in the upper troposphere (above 5-km altitude; Fig. 7a) while reflectivity in specific differential phase behaves likewise with lower median values (Fig. 8a). The size-sorting mechanism is visible from differential reflectivity in convective rainfall areas where the median generally decreases with height in the whole lower troposphere (Fig. 7b) while this mechanism in stratiform rainfall areas is shallower below 2.5-km altitude (Fig. 8b). Analogous to differential reflectivity, the difference of specific differential phase between convective rainfall areas and stratiform rainfall areas mainly occurs in the lower troposphere (Figs. 7c and 8c) and implies the dominance of convective rainbands over rainfall amounts in this super typhoon case. In the upper troposphere, differential reflectivity and specific differential phase have low median values contributed mainly by snow as well as a small portion of higher values contributed mainly by supercooled rainwater and mixed-phase hydrometeors in updraft regions (referring to Wu et al. 2018). Near the melting layer between the lower and upper troposphere, all three variables exhibit relatively dispersed distributions which reflect the presence of complex hydrometeor states (Figs. 7a–c and 8a–c). As for NoDA, reflectivity is generally overestimated except in the lower troposphere of stratiform rainfall areas and the spread is excessive (Figs. 7d and 8d). Differential reflectivity and specific differential phase in convective rainfall areas are also overestimated with an excessive spread in the lower troposphere, especially differential reflectivity (Figs. 7e and f). In the upper troposphere, differential reflectivity and specific differential phase are seriously underestimated as values overwhelmingly near zero because of the limited capability of the Rayleigh scattering approximation in the observation operator to handle ice-phase hydrometeors. Differential reflectivity and specific differential phase in stratiform rainfall areas are generally underestimated except for an unrealistic differential reflectivity spike near the melting layer (Figs. 8e and f), mainly owing to the overestimation that often takes place where mixed-phase hydrometeors are generated with a low total number concentration. In next two subsections, whether these initial observation-space deviations in NoDA at T0 can be mitigated by radar data assimilation is assessed in addition to whether rainfall nowcasting can be improved.

All radar data assimilation experiments are perturbed around the NoDA initial condition at 1200 UTC to share a similar synoptic-scale environment and allow enough time for LETKF assimilation cycles. Coming straight to the point of rainfall nowcast performance, the ranking order from best to worst for the first group of experiments appears to be VK, VZ, V, VD and NoDA according to both root-mean-square error (Fig. 6a) and spatial correlation coefficient (Fig. 6c) statistics of hourly rainfall accumulations. The evolution trends of root-mean-square error curves from different experiments are similar, and so are those of spatial correlation coefficient curves. This indicates that radar data assimilation cycles for a couple of hours cannot alter the evolution trend governed by the synoptic-scale forcing. It is straightforward for the outperformance of V over NoDA, VZ over V, and VK over VZ because: 1) radial velocity is beneficial for three-dimensional wind analyses via a highly-linear correlation, 2) reflectivity provides quantitative information about hydrometeors on top of radial velocity, and 3) specific differential phase is much more linearly proportional to the rain rate than reflectivity. What is surprising is the degradation of VD relative to V, even relative to NoDA during the final 3 hours. This means that assimilating solely differential reflectivity on top of radial velocity, which lacks the information of hydrometeor number concentrations, has a negative impact on rainfall nowcasts even utilizing a double-moment bulk microphyscial scheme. This can be attributed to unreliable ensemble-based background error correlations between differential reflectivity and updated prognostic variables, especially in the upper troposphere where the polarimetric radar observation operator does not handle ice-phase hydrometeors well.

In contrast, assimilating solely reflectivity or specific differential phase on top of radial velocity has a positive effect, and the spatial distributions of analyzed radar variables at T0 and predicted rainfall in VZ and VK are further compared. From the fields at 3.5-km altitude (Fig. 5), the analysis ensemble means for all three variables in VZ and VK exhibit more continuous horizontal distributions as the observations than NoDA. The underestimation north of the eye and overestimation west and south of the eye in NoDA are mitigated in VZ and a little more in VK. From the contoured frequency by altitude diagrams in convective rainfall areas (Fig. 7) and stratiform rainfall areas (Fig. 8), the overestimation and excessive spread of reflectivity for NoDA in both areas are significantly corrected in VZ and VK as well as specific differential phase in the lower troposphere of convective rainfall areas. However, no improvement is seen for specific differential phase elsewhere and differential reflectivity everywhere in VZ and VK (also in VD which is not shown). The major difference between

VZ and VK is the spread of specific differential phase in the lower troposphere of convective rainfall areas, which is more similar to the observations (Fig. 7c) in VK (Fig. 7l) than in VZ (Fig. 7i). With respect to the predicted rainfall (Fig. 3), the underestimation in area A and overestimation in area C for NoDA during the initial 3 hours are notably mitigated in VZ and VK, and the distribution of light rain areas approaches the observed pattern as well. During the final 3 hours, the positive effect of radar data assimilation decays, also shown in the root-mean-square error and spatial correlation coefficient statistics (Figs. 6a and c). As for the advantage of VK over VZ, the superior accuracy of specific differential phase in the lower troposphere of convective rainfall areas conduces to better rainfall nowcast performance mainly in the heavy rainfall areas closely observed by RCWF, which is demonstrated by the distribution of improvement in VK over VZ (Figs. 3m–o) while absolute rainfall patterns look indistinguishable between both experiments (Figs. 3g–l).

The assimilation of conventional radial velocity and reflectivity observations has become operational in modern convective-scale forecasting systems; thus, the second group of experiments, NoDA, VZ, VZD, VZK, and VZDK, are compared to examine if further rainfall nowcast improvement is achievable by assimilating differential reflectivity and/or specific differential phase on top of the assimilation of both radial velocity and reflectivity. Coming straight to the root-mean-square error and spatial correlation coefficient statistics of hourly rainfall accumulations (Figs. 6b and d), the ranking order from best to worst appears to VZK, VZDK, VZ, VZD, and NoDA despite limited differences between VZK and VZDK as well as between VZ and VZD. This means that the additional assimilation of specific differential phase still brings significant rainfall nowcast improvement on top of radial velocity and reflectivity, and the aforementioned negative impact of differential reflectivity is less influential when reflectivity is assimilated to provide indirect information of hydrometeor number concentrations. Furthermore, the performance in VZK (magenta thick curves in Figs. 6b and d) is close to that in VK (magenta thin curves in Figs. 6a and c), which indicates that the assimilation of reflectivity is negligible to save computational costs in the aspect of operation if specific differential phase that contains more complete hydrometeor information is assimilated.

6. Conclusions

This study refines the WRF-LETKF radar assimilation system originally developed in Tsai et al. (2014), by incorporating a polarimetric radar observation operator for the purpose of investigating the sensitivities of deterministic rainfall nowcast performance to polarimetric radar data assimilation in a real super typhoon case. A series of radar data assimilation experiments and a NoDA control experiment under similar synoptic-scale forcing are carried out and verified against the observations of the RCWF S-band polarimetric radar and surface rain gauges. The results are summarized as follows: 1) all radar data assimilation experiments have better rainfall nowcast performance than NoDA within the coverage of RCWF, especially during the initial 3 hours of the deterministic nowcast, but cannot alter the evolution trend governed by the synoptic-scale forcing, 2) assimilating specific differential phase, which contains more complete hydrometeor information and a more linear relation to the rain rate, results in more accurate specific differential phase analyses in the lower troposphere and consequent rainfall nowcasts in convective rainfall areas than assimilating reflectivity, 3) assimilating solely specific differential phase on top of radial velocity, which lacks the information of hydrometeor number concentrations, degrades rainfall nowcast performance because of unreliable background error correlations between differential reflectivity and updated variables especially in the upper troposphere where the observation operator does not handle ice-phase hydrometeors well, and 4) on top of assimilating both radial velocity and reflectivity, the additional assimilation of specific differential phase still brings significant rainfall nowcast improvement and the negative impact of differential reflectivity is less influential.

References

Brown, B. R., M. M. Bell, and A. J. Frambach, 2016: Validation of simulated hurricane drop size distributions using polarimetric radar. *Geophys. Res. Lett.*, **43**, 910–917, doi: 10.1002/2015GL067278.

Hunt, B. R., E. J. Kostelich, and I. Szunyogh, 2007: Efficient data assimilation for spatiotemporal chaos: a local ensemble transform Kalman filter. *Physica D*, **230**, 112–126, doi: 10.1016/j.physd.2006.11.008.

Jung, Y., G. Zhang, and M. Xue, 2008a: Assimilation of simulated polarimetric radar data for a convective storm using the ensemble Kalman filter. Part I: Observation operators for reflectivity and polarimetric variables. *Mon. Wea. Rev.*, **136**, 2228–2245, doi: 10.1175/2007MWR2083.1.

Jung, Y., M. Xue, G. Zhang, and J. M. Straka, 2008b: Assimilation of simulated polarimetric radar data for a convective storm using the ensemble Kalman filter. Part II: Impact of polarimetric data on storm analysis. *Mon. Wea. Rev.*, **136**, 2246–2260, doi: 10.1175/2007MWR2288.1.

Putnam, B. J., M. Xue, Y. Jung, G. Zhang, and F. Kong, 2017a: Simulation of polarimetric radar variables from 2013 CAPS spring experiment storm-scale ensemble forecasts and evaluation of microphysics schemes. *Mon. Wea. Rev.*, **145**, 49–73, doi: 10.1175/MWR-D-15-0415.1.

Putnam, B. J., M. Xue, Y. Jung, N. A. Snook, and G. Zhang, 2017b: Ensemble probabilistic prediction of a mesoscale convective system and associated polarimetric radar variables using single-moment and double-moment microphysics schemes and EnKF radar data assimilation. *Mon. Wea. Rev.*, **145**, 2257–2279, doi: 10.1175/MWR-D-16-0162.1.

Putnam, B., M. Xue, Y. Jung, N. Snook, and G. Zhang, 2019: Ensemble Kalman filter assimilation of polarimetric radar observations for the 20 May 2013

Oklahoma tornadic supercell case. *Mon. Wea. Rev.*, **147**, 2511–2533, doi: 10.1175/MWR-D-18-0251.1.

Tsai, C.-C., S.-C. Yang, and Y.-C. Liou, 2014: Improving quantitative precipitation nowcasting with a local ensemble transform Kalman filter radar data assimilation system: Observing system simulation experiments. *Tellus A*, **66**, 21804, doi: 10.3402/tellusa.v66.21804.

Wu, D., K. Zhao, M. R. Kumjian, X. Chen, H. Huang, M. Wang, A. C. Didlake Jr., Y. Duan, and F. Zhang, 2018: Kinematics and microphysics of convection in the outer rainband of Typhoon Nida (2016) revealed by polarimetric radar. *Mon. Wea. Rev.*, **146**, 2147–2159, doi: 10.1175/MWR-D-17-0320.1.

Table 1. The list of radar data assimilation experiments.

Name	Assimilated radar variables
NoDA	None
V	V_r
VZ	V_r and Z_H
VD	V_r and Z_{DR}
VK	V_r and K_{DP}
VZD	V_r, Z_H, and Z_{DR}
VZK	V_r, Z_H, and K_{DP}
VZDK	V_r, Z_H, Z_{DR}, and K_{DP}

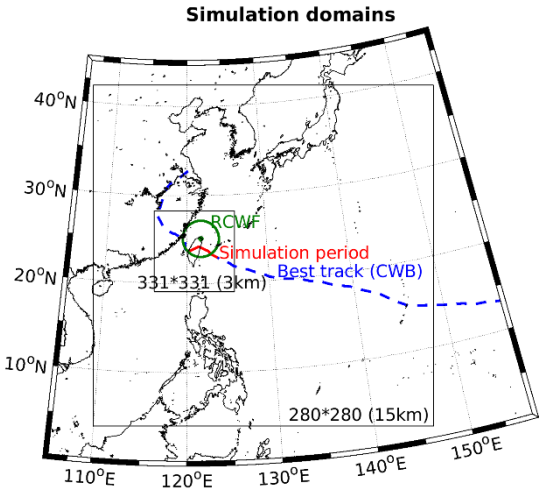

Fig. 1. The simulation domains of the two grids with two-way nesting. The green dot and circle mark the location and maximum unambiguous range of RCWF. The blue dashed line is the best track of Soudelor analyzed by CWB, where the red solid segment represents the simulation period in this study during 1200 UTC 7 August – 0200 UTC 8 August.

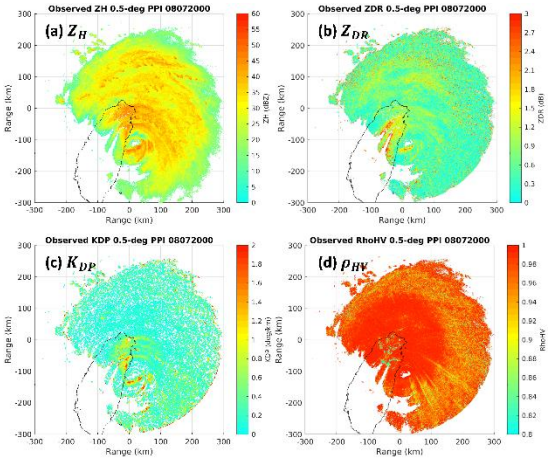

Fig. 2. The (a) Z_H, (b) Z_{DR}, (c) K_{DP}, and (d) ρ_{HV} PPI observations of RCWF at a 0.5-deg elevation angle at 2000 UTC 7 August.

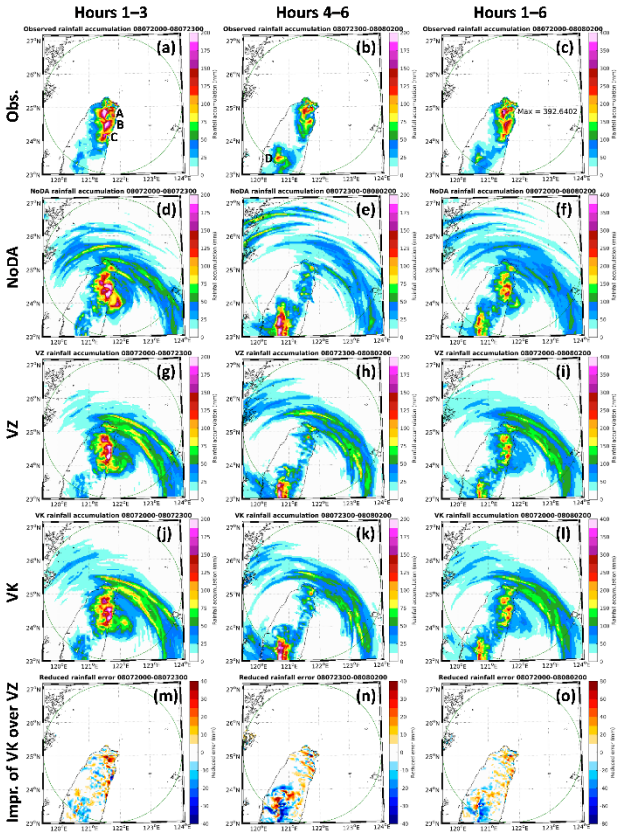

Fig. 3. The rainfall accumulations observed by surface rain gauges during (a) 2000–2300 UTC 7 August, (b) 2300 UTC 7 August – 0200 UTC 8 August, and (c) 2000 UTC 7 August – 0200 UTC 8 August. The green circle marks the maximum unambiguous range of RCWF. Uppercase A, B, C, and D mark the discussed heavy rainfall areas. The rainfall accumulation counterparts for the nowcasts in (d–f) NoDA, (g–i) VZ, and (j–l) VK are compared, and the improvement in VK over VZ is shown in (m–o).

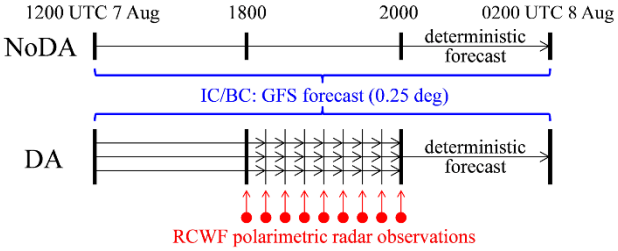

Fig. 4. The schematic design of polarimetric radar data assimilation experiments.

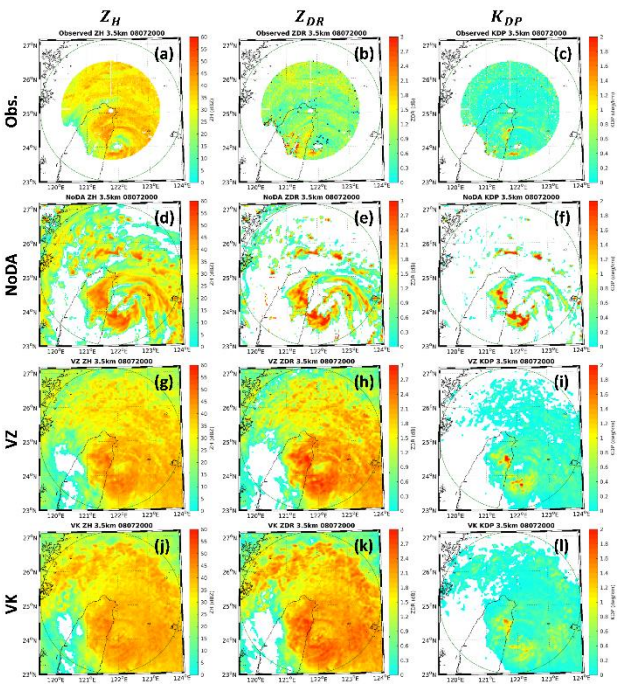

Fig. 5. The (a) Z_H, (b) Z_{DR}, and (c) K_{DP} observations of RCWF at 3.5-km altitude at 2000 UTC 7 August. The green circle marks the maximum unambiguous range of RCWF. The Z_H, Z_{DR}, and K_{DP} counterparts for the (d–f) nowcast in NoDA, (g–i) analysis ensemble mean in VZ, and (j–l) analysis ensemble mean in VK are compared.

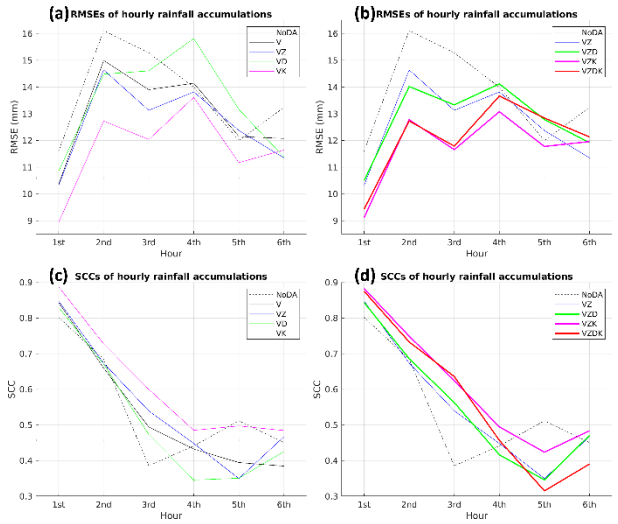

Fig. 6. The (a and b) root-mean-square errors and (c and d) spatial correlation coefficients of hourly rainfall accumulations against observed rainfall within the maximum unambiguous range of RCWF for the nowcasts in NoDA, V, VZ, VD, VK, VZD, VZK, and VZDK during 2000 UTC 7 August – 0200 UTC 8 August.

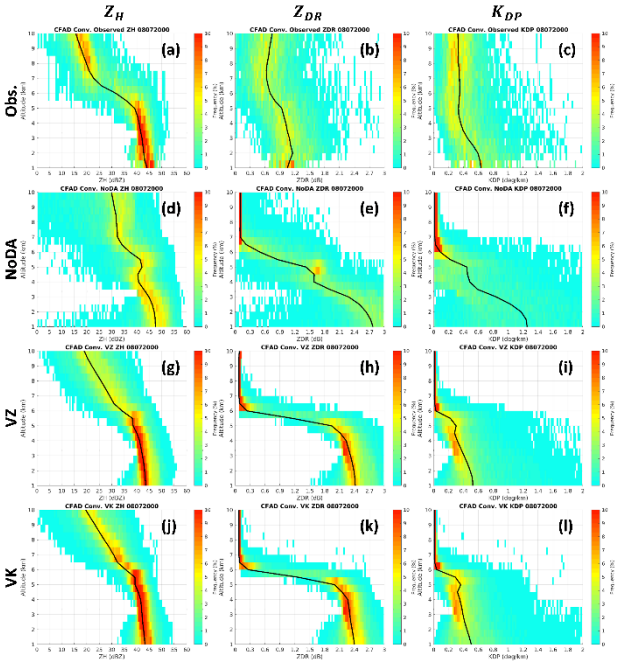

Fig. 7. The contoured frequency by altitude diagrams in convective rainfall areas (Z_H > 40 dBZ at 3-km altitude) for the (a) Z_H, (b) Z_{DR}, and (c) K_{DP} observations of RCWF at 2000 UTC 7 August. The contoured frequency by altitude diagram counterparts confined to a cylindrical volume within the maximum unambiguous range of RCWF for the (d–f) nowcast in NoDA, (g–i) analysis ensemble mean in VZ, and (j–l) analysis ensemble mean in VK are compared.

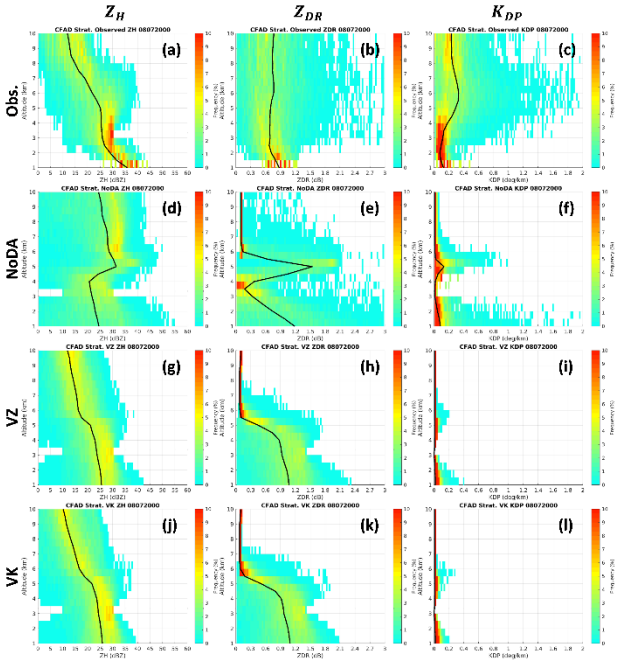

Fig. 8. The contoured frequency by altitude diagrams as in Fig. 7, but in stratiform rainfall areas (10 dBZ < Z_H < 30 dBZ at 3-km altitude).